PHYSICAL REVIEW D **80,** 053009 (2009)

Bayesian constraints on ϑ_{13} from solar and KamLAND neutrino data

H. L. Ge,[1] C. Giunti,[2] and Q. Y. Liu[1]

[1]*Department of Modern Physics, University of Science and Technology of China, Hefei, Anhui 230026, China*
[2]*INFN, Sezione di Torino, Via P. Giuria 1, I10125 Torino, Italy*

(Received 30 October 2008; published 21 September 2009)

We present the results of a Bayesian analysis of solar and KamLAND neutrino data in the framework of three-neutrino mixing. We adopt two approaches for the prior probability distribution of the oscillation parameters Δm^2_{21}, $\sin^2\vartheta_{12}$, $\sin^2\vartheta_{13}$: (1) a traditional flat uninformative prior; and (2) an informative prior which describes the limits on $\sin^2\vartheta_{13}$ obtained in atmospheric and long-baseline accelerator and reactor neutrino experiments. In both approaches, we present the allowed regions in the $\sin^2\vartheta_{13}$-Δm^2_{21} and $\sin^2\vartheta_{12}$-$\sin^2\vartheta_{13}$ planes, as well as the marginal posterior probability distribution of $\sin^2\vartheta_{13}$. We confirm the 1.2σ hint of $\vartheta_{13} > 0$ found in [G. Fogli *et al.*, Phys. Rev. Lett. **101**, 141801 (2008).] from the analysis of solar and KamLAND neutrino data. We found that the statistical significance of the hint is reduced to about 0.8σ by the constraints on $\sin^2\vartheta_{13}$ coming from atmospheric and long-baseline accelerator and reactor neutrino data, in agreement with [T. Schwetz, M. Tortola, and J. W. F. Valle, New J. Phys. **10**, 113011 (2008).].

DOI: 10.1103/PhysRevD.80.053009 PACS numbers: 14.60.Pq, 26.65.+t, 14.60.Lm, 02.50.Tt

I. INTRODUCTION

Neutrino oscillation experiments have shown that neutrinos are massive and mixed particles (see Refs. [1–3]). Solar and KamLAND neutrino experiments observed $\overset{(-)}{\nu}_e \to \overset{(-)}{\nu}_{\mu,\tau}$ transitions due to neutrino oscillations generated by a squared-mass difference

$$\Delta m^2_{\rm SOL} \simeq 8 \times 10^{-5}\ {\rm eV}^2. \tag{1.1}$$

Atmospheric and long-baseline accelerator neutrino experiments measured $\overset{(-)}{\nu}_\mu \to \overset{(-)}{\nu}_\tau$ transitions due to neutrino oscillations generated by a squared-mass difference

$$\Delta m^2_{\rm ATM} \simeq 2.5 \times 10^{-3}\ {\rm eV}^2. \tag{1.2}$$

Hence, there is a hierarchy of squared-mass differences:

$$\Delta m^2_{\rm ATM} \simeq 30 \Delta m^2_{\rm SOL}. \tag{1.3}$$

This hierarchy is easily accommodated in the framework of three-neutrino mixing, in which there are two independent squared-mass differences. We label the neutrino masses in order to have

$$\Delta m^2_{\rm SOL} \equiv \Delta m^2_{21}, \tag{1.4}$$

$$\Delta m^2_{\rm ATM} \simeq |\Delta m^2_{31}| \simeq |\Delta m^2_{32}|. \tag{1.5}$$

The two possible schemes are illustrated in Fig. 1. They differ by the sign of $\Delta m^2_{31} \simeq \Delta m^2_{32}$.

For the 3×3 unitary mixing matrix of neutrinos we adopt the standard parametrization in Eq. (A2) of Appendix A [4,5]. The negative results of the Chooz [6] and Palo Verde [7] long-baseline neutrino oscillation experiments, together with the evidence of neutrino oscillations in atmospheric and long-baseline accelerator neutrino experiments, imply that the mixing angle ϑ_{13} is small [8] (see Ref. [9] for updated bounds). On the other hand, the values of the other two mixing angles are known to be large from the results of solar and KamLAND experiments (ϑ_{12}) and the results of atmospheric and long-baseline accelerator neutrino experiments (ϑ_{23}).

In Ref. [10] we presented the results of a Bayesian analysis of the solar and KamLAND neutrino data in the framework of two-neutrino mixing, which is obtained from three-neutrino mixing in the approximation of negligible ϑ_{13}. In this paper, we extend our Bayesian analysis to the framework of three-neutrino mixing, aiming at the determination of the constraints on the value of the small mixing angle ϑ_{13} implied by solar and KamLAND neutrino data.

The plan of the paper is as follows. In Sec. II we present the constraints on the value of ϑ_{13} in a standard χ^2 analysis, to be compared with the Bayesian results with an

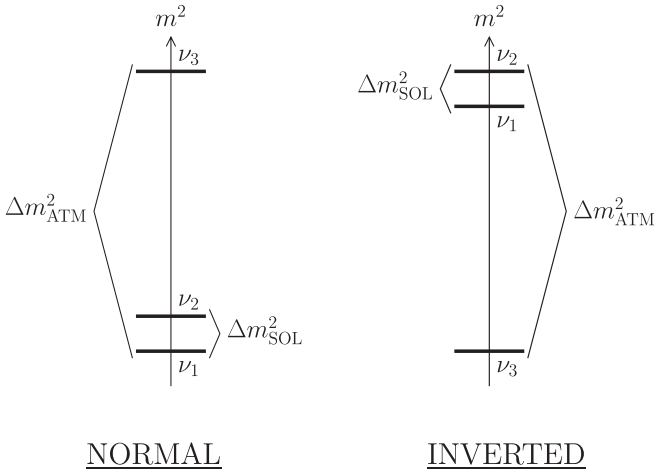

FIG. 1. The two three-neutrino schemes allowed by the hierarchy $\Delta m^2_{\rm SOL} \ll \Delta m^2_{\rm ATM}$.

uninformative prior presented in Sec. III. In Sec. IV we present the results obtained with an informative prior which represents information on ϑ_{13} obtained in atmospheric and long-baseline accelerator and reactor neutrino experiments, independently from solar and KamLAND neutrino data. The conclusions are given in Sec. V.

II. χ^2 ANALYSIS

The traditional way to extract information on the neutrino mixing parameters from solar neutrino data is based on the standard least-squares method, also called "χ^2 analysis." The least-squares function χ^2 is given by $\chi^2 = -2\ln\mathcal{L} + \text{constant}$, where $\mathcal{L}$ is the likelihood function. In this section we present our results in a traditional least-squares analysis of solar and KamLAND neutrino data. The least-squares function described in this section will be used in the Bayesian analysis presented in Sec. III for the calculation of the sampling probability distribution, which is proportional to the likelihood function.

We consider the data of the following solar neutrino experiments: Homestake [11], GALLEX/GNO [12], SAGE [13], Super-Kamiokande [14,15], and SNO [16]. The least-squares function of solar neutrino data is given by

$$\chi^2_S = \sum_{i,j=1}^{N_S} (R_i^{\rm exp} - R_i^{\rm th})(V_S^{-1})_{ij}(R_j^{\rm exp} - R_j^{\rm th}). \qquad (2.1)$$

Here $R_i^{\rm exp}$ are the solar data points, whose number is $N_S = 80$, accounted as follows:

(i) the rate of the Homestake ^{37}Cl experiment [11];
(ii) the combined rate of the ^{71}Ga experiments GALLEX/GNO [12] and SAGE [13];
(iii) the day and night energy spectra of the Super-Kamiokande experiment [14] (21 + 21 bins) and Super-Kamiokande experiment [15];
(iv) the day and night energy spectra of charged-current events in the SNO experiment [16] (17 + 17 bins);
(v) the neutral-current event rate in the salt phase of the SNO experiment [16];
(vi) the neutral-current detection array neutral-current event rate in the SNO experiment [17].

The corresponding theoretical rates $R_i^{\rm th}$ depend on the neutrino oscillation parameters. The covariance error matrix V_S takes into account the correlations of theoretical uncertainties, according to the discussions in Refs. [18–21]. In our analysis, the initial flux of ^{8}B solar neutrinos is considered as a free parameter to be determined by the fit, mainly through the SNO neutral-current data. For the other solar neutrino fluxes, we assume the BP04 standard solar model [22]. The transition probability in the Sun is calculated using the standard method [23] based on the hierarchy of squared-mass differences in Eq. (1.3), which implies that the oscillations generated by the large mass-squared difference $\Delta m^2_{\rm ATM}$ are averaged out (see Refs. [1–3]). For the calculation of the regeneration of solar ν_e's in the Earth, we use Eq. (A12), derived in Appendix A.

Neutrino oscillations due to the same mixing parameters which generate the oscillations of solar neutrinos have been observed in the KamLAND very-long-baseline reactor neutrino oscillation experiment [24]. The KamLAND least-squares function is[1]

$$\chi^2_S = \sum_{i,j=1}^{N_K} (N_i^{\rm exp} - N_i^{\rm th})(V_K^{-1})_{ij}(N_j^{\rm exp} - N_j^{\rm th}), \qquad (2.2)$$

where $N_K = 17$ is the number of energy bins, $N_i^{\rm exp}$ is the number of events measured in the ith bin and N_i^{th} is the corresponding theoretical value, which depends on the neutrino oscillation parameters. The covariance error matrix V_K takes into account the statistical uncertainties and the correlated and uncorrelated systematic uncertainties, all added in quadrature.

The global least-squares function is

$$\chi^2_T = \chi^2_S + \chi^2_K. \qquad (2.3)$$

We minimized χ^2_T with respect to the three mixing parameters Δm^2_{21}, $\sin^2\vartheta_{12}$, and $\sin^2\vartheta_{13}$. We found the best-fit point

$$\Delta m^2_{21} = 7.58\times10^{-5}\ \text{eV}^2, \qquad \sin^2\vartheta_{12} = 0.31, \qquad \sin^2\vartheta_{13} = 0.021. \qquad (2.4)$$

The 90%, 95%, and 99.73% C.L. regions in the $\sin^2\vartheta_{13}$-Δm^2_{21} and $\sin^2\vartheta_{12}$-$\sin^2\vartheta_{13}$ planes are shown, respectively, in Figs. 2 and 3. These regions correspond to 2 degrees of freedom. The third parameter (ϑ_{12} in Fig. 2 and Δm^2_{12} in Fig. 3) is marginalized by minimizing χ^2_T.

From Figs. 2 and 3, one can see that KamLAND data constrain ϑ_{13} more than solar data.

Figure 4 shows the difference $\Delta\chi^2$ of χ^2 from its minimum value as a function of $\sin^2\vartheta_{13}$. The resulting 90%, 95%, and 99.73% C.L. upper bounds for $\sin^2\vartheta_{13}$, determined by the intersection of the $\Delta\chi^2$ curve with the straight horizontal lines in Fig. 4, are, respectively,

$$\sin^2\vartheta_{13} < 0.051(90\%), \qquad 0.057(95\%), \qquad 0.076(99.73\%). \qquad (2.5)$$

It is interesting to note that the best-fit point for $\sin^2\vartheta_{13}$ in Eq. (2.4) is slightly larger than zero, in agreement with the value obtained in Ref. [27] (see also Refs. [9,28]), $\sin^2\vartheta_{13} = 0.021 \pm 0.017$. Since we have $\sin^2\vartheta_{13} = 0.021 \pm 0.018$, our hint of $\vartheta_{13} > 0$ is at the 1.2σ level

[1] In Ref. [10] and in the first version of this paper (arXiv:0810.5443v1) we adopted a different least-squares function, which is appropriate for a Poisson distribution (see Refs. [5,25]). We think that the Gaussian least-squares function in Eq. (2.2) is more appropriate for the analysis of KamLAND data, because it allows us to take into account the systematic uncertainty in each energy bin, as discussed in Ref. [26].

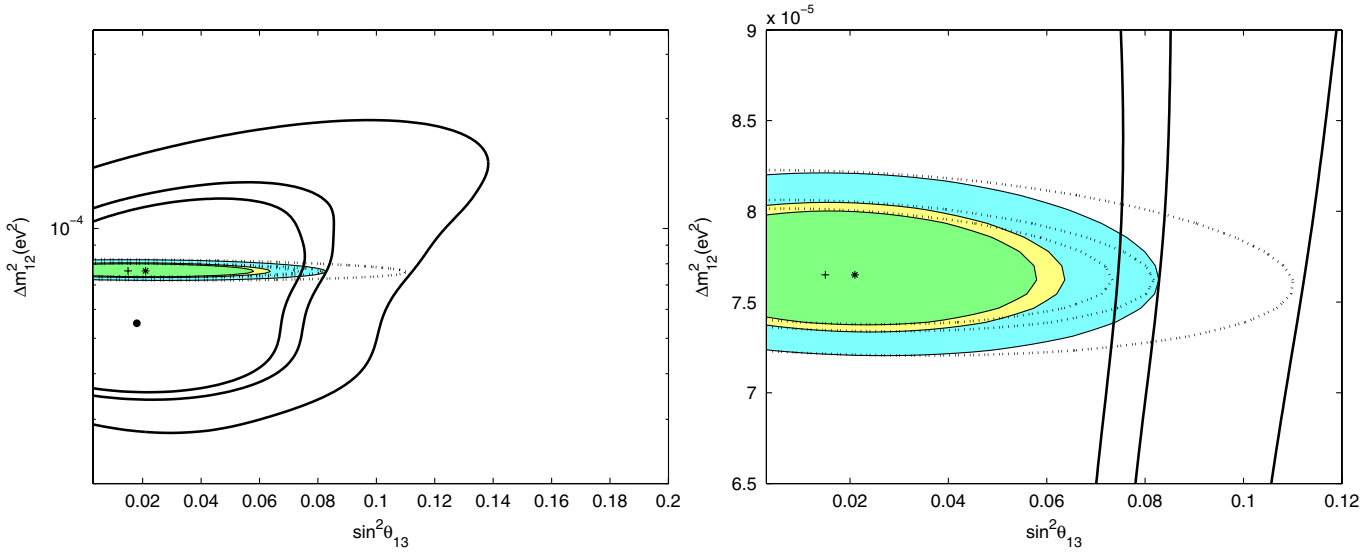

FIG. 2 (color online). The 90%, 95%, and 99.73% C.L. regions in the $\sin^2\vartheta_{13}$-Δm^2_{21} plane obtained in the least-squares analysis. The solid and dotted lines enclose, respectively, the regions obtained with solar data and KamLAND data. The shadowed areas are obtained from the combined analysis of solar and KamLAND data. The figure on the right is an enlargement of the interesting area of the figure on the left. The dot, cross, and asterisk indicate, respectively, the best-fit points of the solar, KamLAND, and combined analyses.

(the precise value of $\Delta\chi^2$ for $\vartheta_{13} = 0$ is 1.33, corresponding to 1.15σ).

III. BAYESIAN ANALYSIS

In the Bayesian approach, the analysis of the data allows us to calculate the posterior probability distribution of the mixing parameters, assuming a prior probability distribution which quantifies the prior knowledge. Denoting with $\mathcal{M} = \{\Delta m^2_{21}, \sin^2\vartheta_{12}, \sin^2\vartheta_{13}\}$ the set of mixing parameters to be determined by the analysis, the normalized posterior probability distribution of the mixing parameters is given by

$$p(\mathcal{M}|\mathcal{D}, \mathcal{I}) = \frac{p(\mathcal{D}|\mathcal{M}, \mathcal{I})p(\mathcal{M}|\mathcal{I})}{\int d\mathcal{M} p(\mathcal{D}|\mathcal{M}, \mathcal{I})p(\mathcal{M}|\mathcal{I})}, \qquad (3.1)$$

where $p(\mathcal{D}|\mathcal{M}, \mathcal{I})$ is the sampling probability distribution, $p(\mathcal{M}|\mathcal{I})$ is the prior probability distribution, and $d\mathcal{M} \equiv d\Delta m^2_{21} d\sin^2\vartheta_{12} d\sin^2\vartheta_{13}$. The symbols $\mathcal{D}$ and $\mathcal{I}$ represent,

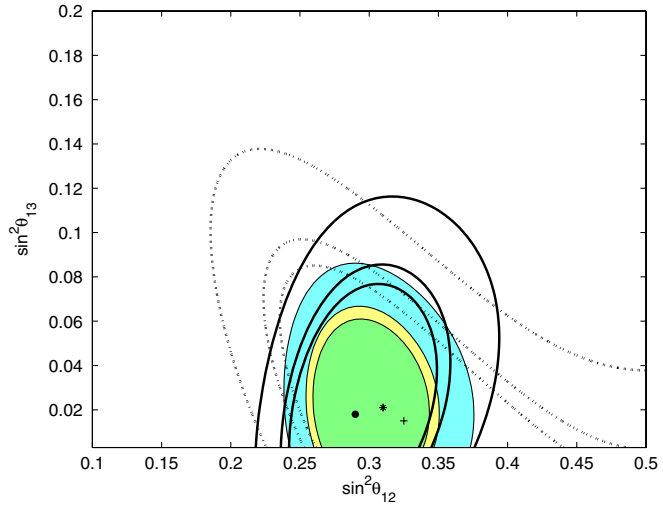

FIG. 3 (color online). The 90%, 95%, and 99.73% C.L. regions in the $\sin^2\vartheta_{12}$-$\sin^2\vartheta_{13}$ plane obtained in the least-squares analysis. The solid and dotted lines enclose, respectively, the regions obtained with solar data and KamLAND data. The shadowed areas are obtained from the combined analysis of solar and KamLAND data. The dot, cross, and asterisk indicate, respectively, the best-fit points of the solar, KamLAND, and combined analyses.

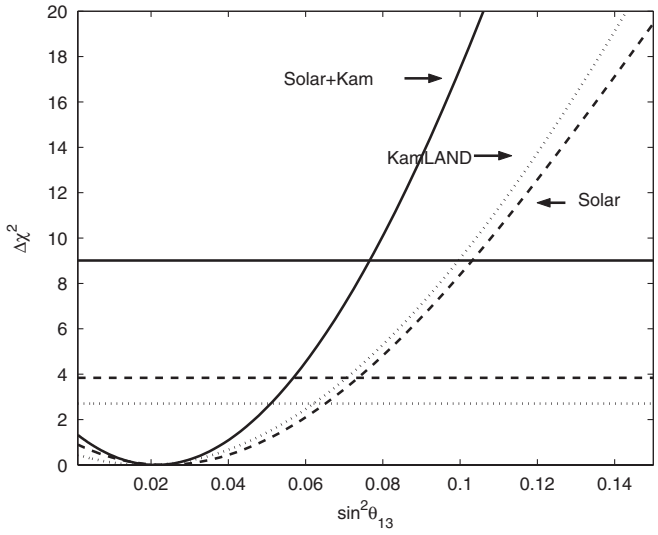

FIG. 4. $\Delta\chi^2$ as a function of $\sin^2\vartheta_{13}$. The straight horizontal lines show the levels corresponding to 90%, 95%, and 99.73% C.L.

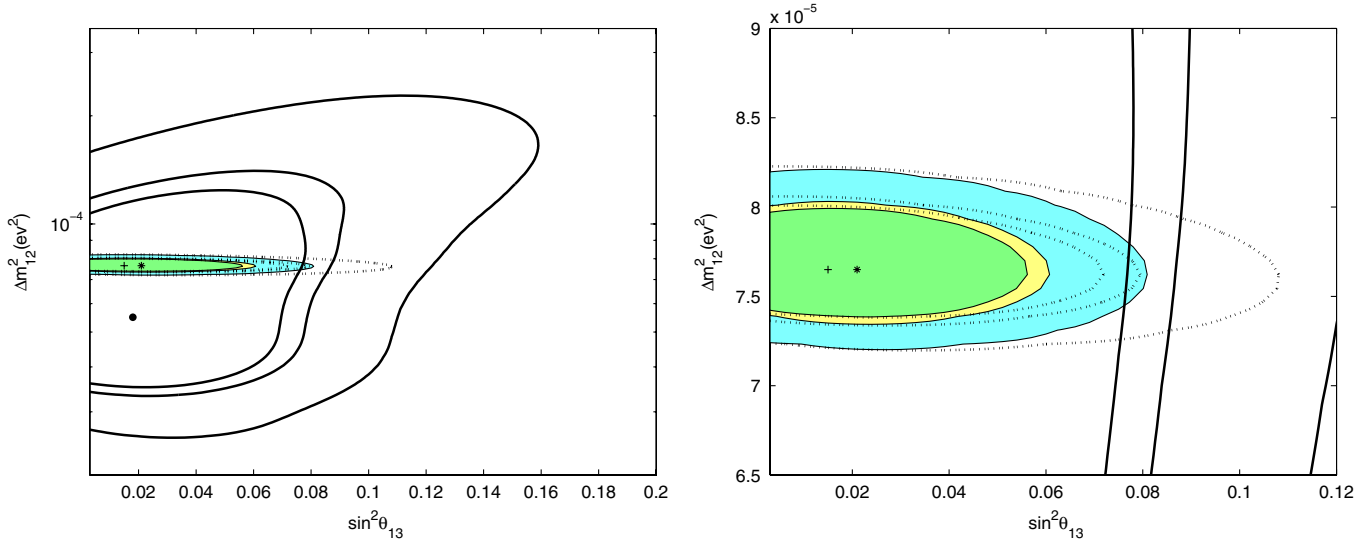

FIG. 5 (color online). The 90%, 95%, and 99.73% Bayesian credible regions in the $\sin^2\vartheta_{13}$-Δm^2_{21} plane obtained with an uninformative constant prior probability distribution. The solid and dotted lines enclose, respectively, the credible regions obtained with solar data and KamLAND data. The shadowed areas are obtained from the combined analysis of solar and KamLAND data. The figure on the right is an enlargement of the interesting area of the figure on the left. The dot, cross, and asterisk indicate, respectively, the best-fit points of the solar, KamLAND, and combined analyses.

respectively, the experimental data and all the prior general knowledge and assumptions on solar and neutrino physics.

The sampling probability distribution is given by

$$p(\mathcal{D}|\mathcal{M}, I) \propto (|V_S||V_K|)^{-1/2} e^{-\chi^2_T/2}, \tag{3.2}$$

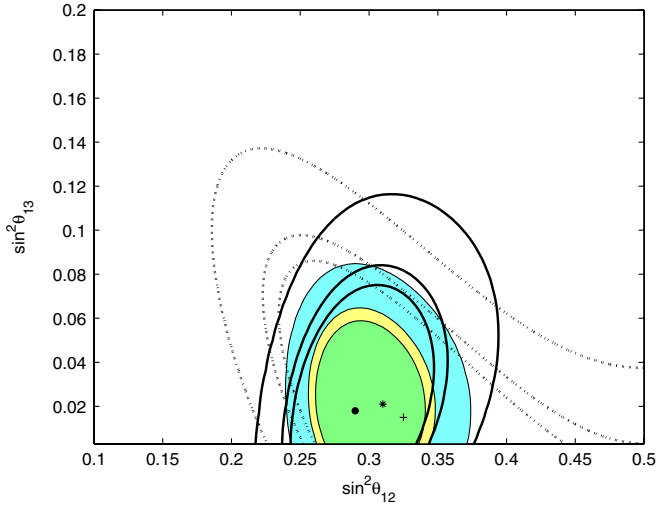

FIG. 6 (color online). The 90%, 95%, and 99.73% Bayesian credible regions in the $\sin^2\vartheta_{12}$-$\sin^2\vartheta_{13}$ plane obtained with an uninformative constant prior probability distribution. The solid and dotted lines enclose, respectively, the regions obtained with solar data and KamLAND data. The shadowed areas are obtained from the combined analysis of solar and KamLAND data. The dot, cross, and asterisk indicate, respectively, the best-fit points of the solar, KamLAND, and combined analyses.

with the least-squares function χ^2_T given in Eq. (2.3). The normalization factor is irrelevant, since it cancels in Eq. (3.1). We retained only the coefficient $(|V_S||V_K|)^{-1/2}$, which depends on the neutrino mixing parameters in $\mathcal{M}$ (see Ref. [21]).

In Ref. [10] we have shown that the choices of constant uninformative priors in the $\sin^2\vartheta_{12}$-Δm^2_{21} or $\log\sin^2\vartheta_{12}$-$\log\Delta m^2_{21}$ planes are practically equivalent, because of the excellent quality of the data. Hence, in the three-neutrino mixing analysis we assume a constant prior in the three-dimensional space of the parameters Δm^2_{21}, $\sin^2\vartheta_{12}$, and $\sin^2\vartheta_{13}$.

Figures 5 and 6 show the resulting credible regions with 90%, 95%, and 99.73% probability in the $\sin^2\vartheta_{13}$-Δm^2_{21} and $\sin^2\vartheta_{12}$-$\sin^2\vartheta_{13}$ planes, respectively. A credible region is the smallest region with the given integral posterior probability. In practice, a credible region is calculated as the two-dimensional region surrounded by an isoprobability contour which contains the point of highest posterior probability. In each plane of parameters, the probability distribution is calculated by integrating $p(\mathcal{M}|\mathcal{D}, I)$ over the third parameter ($\sin^2\vartheta_{12}$ in the plane $\sin^2\vartheta_{13}$-Δm^2_{21} and Δm^2_{12} in the plane $\sin^2\vartheta_{12}$-$\sin^2\vartheta_{13}$).

The credible regions in Figs. 5 and 6 are similar but slightly lager than the χ^2-allowed regions in Figs. 2 and 3. The comparison of the two types of region is shown in Fig. 7 and 8. It is fair to conclude that the Bayesian analysis with an uninformative prior confirms the results obtained with the traditional χ^2 analysis.

Figure 9 shows the marginal posterior probability distribution of $\sin^2\vartheta_{13}$, which is given by

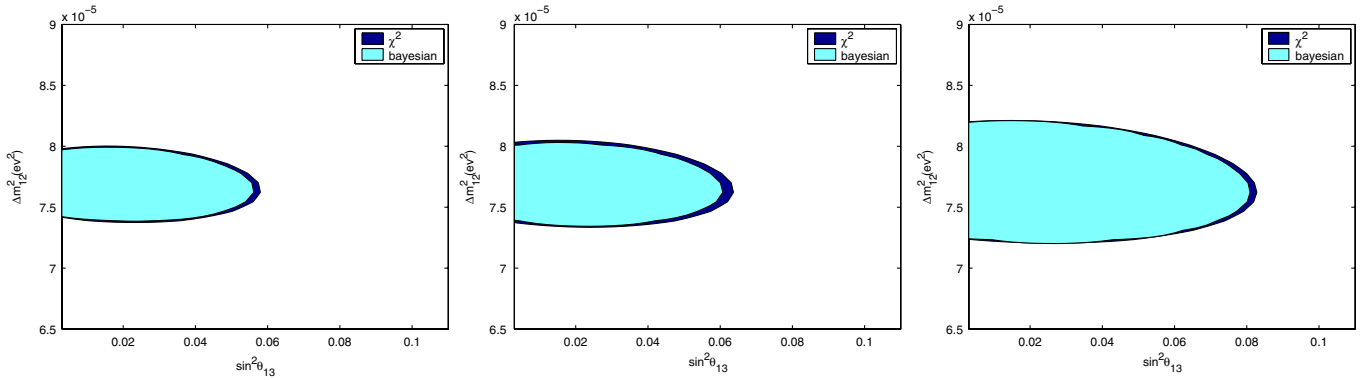

FIG. 7 (color online). Comparison of the allowed regions in the $\sin^2\vartheta_{13}$-Δm^2_{21} plane obtained with the χ^2 analysis and the Bayesian approach. The light-shadowed and light + dark-shadowed areas cover, respectively, the Bayesian credible regions with ξ probability and the χ^2 region with ξ C.L. In the three figures, from left to right, $\xi = 90\%, 95\%, 99.73\%$.

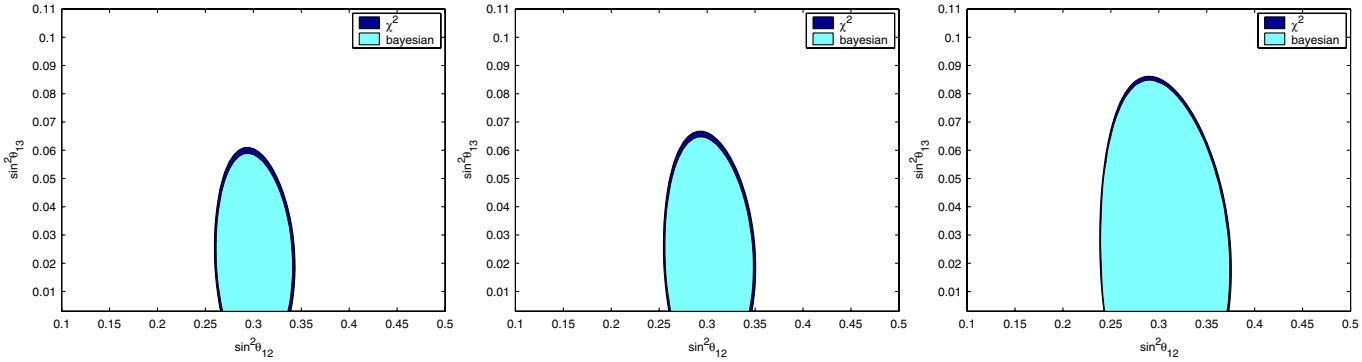

FIG. 8 (color online). Comparison of the allowed regions in the $\sin^2\vartheta_{12}$-$\sin^2\vartheta_{13}$ plane obtained with the χ^2 analysis and the Bayesian approach. The light-shadowed and light + dark − shadowed areas cover, respectively, the Bayesian credible regions with ξ probability and the χ^2 region with ξ C.L. In the three figures, from left to right, $\xi = 90\%, 95\%, 99.73\%$.

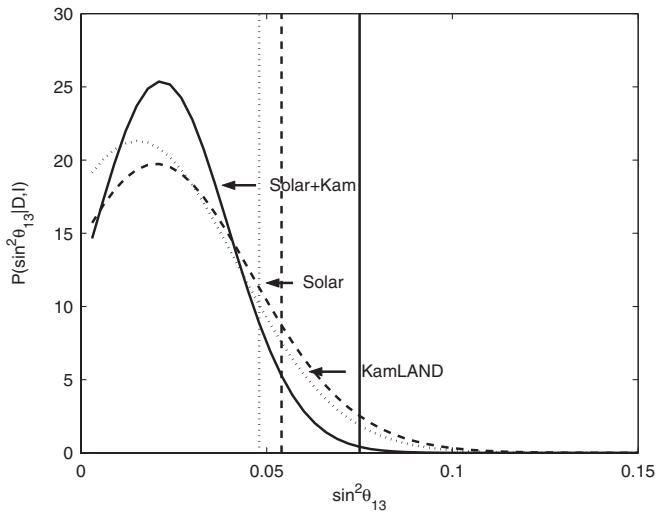

FIG. 9. Marginal posterior probability distribution of $\sin^2\vartheta_{13}$ obtained with an uninformative constant prior probability distribution. The straight vertical lines show the levels of 90%, 95%, and 99.73% integrated probability.

$$p(\sin^2\vartheta_{13}|\mathcal{D}, I) = \int d\Delta m^2_{21} \int d\sin^2\vartheta_{12}\, p(\mathcal{M}|\mathcal{D}, I). \tag{3.3}$$

The resulting credible upper bounds for $\sin^2\vartheta_{13}$ with 90%, 95%, and 99.73% probability are, respectively,

$$\sin^2\vartheta_{13} < 0.048(90\%), \quad 0.054(95\%), \quad 0.075(99.73\%). \tag{3.4}$$

These limits are similar to those in Eq. (2.5), in agreement with the above conclusion that an uninformative-prior Bayesian analysis confirms the results obtained with a χ^2 analysis.

We investigated also the hint of $\vartheta_{13} > 0$ in the Bayesian approach. Since the probability of the smallest posterior credible region which includes $\vartheta_{13} = 0$ is 0.86, considering the rescaled probability corresponding to a two-tailed posterior Gaussian distribution we obtain a hint of $\vartheta_{13} > 0$ at the 1.2σ level, as in the χ^2 analysis (see the discussion at the end of Sec. II).

As a caveat on the comparison of frequentist and Bayesian results, let us remind that the two theories are based on different definitions of probability. Hence, although "numerical results tend to be the same for the two approaches in the asymptotic regime, that is, when there are a lot of data, and statistical uncertainties are small compared with the distance to the nearest physical boundary" [29], the interpretation is different.

In the frequentist theory the probability of a class of random events is the relative frequency of occurrence of these events when the total number of events tends to infinity. In parameter estimation, a confidence interval with α C.L. is an element of a hypothetical set of confidence intervals which have a frequentist probability α of covering the true value of the parameter (see Refs. [29,30]). Notice that in frequentist statistics it is not allowed to make any statement about the true value of the parameter, which is a fixed unknown number, not a random variable, albeit in practice frequentist statistics is very often applied to quantities which are not random variables, as systematic errors. The correct frequentist statements in parameter estimation concern intervals in the parameter space and the frequency of their coverage of the unknown true value in the asymptotic limit. This is the meaning of the allowed regions in Figs. 2 and 3. The 1.2σ hint of $\vartheta_{13} > 0$ discussed at the end of Sec. II means that the best-fit value of $\sin^2\vartheta_{13}$ is 1.2σ away from $\sin^2\vartheta_{13} = 0$, i.e. the confidence intervals obtained in the χ^2 analysis with less than about 76% C.L. do not include $\sin^2\vartheta_{13} = 0$.

In the Bayesian theory probability represents the degree of belief based on the available knowledge. Hence it is possible to estimate a probability for any kind of event, not only for random variables as in frequentist statistics. In particular, systematic errors can be treated without any inconsistency. Moreover, there is no need to consider hypothetical quantities, since the posterior probability distribution is straightforwardly obtained from the prior probability distribution and the sampling probability distribution using Bayes' theorem, as in Eq. (3.1). The only difficult task in Bayesian theory probability is the estimation of the prior probability distribution on the basis of the available knowledge. In parameter estimation, one can calculate the Bayesian probability of the true value of the parameter to lie in an interval by integrating the posterior probability distribution. The 1.2σ hint of $\vartheta_{13} > 0$ discussed above means that the credible intervals obtained with a Gaussian approximation of the posterior probability density having less than about 76% probability do not include $\sin^2\vartheta_{13} = 0$. Note that the Gaussian approximation of the posterior probability density is defined on the whole real axis of $\sin^2\vartheta_{13}$ for the comparison with the analogous frequentist result using the traditional terminology. In fact, the least-squares analysis leads to correct frequentist confidence intervals only in the case of a Gaussian likelihood in which the mean values of the data points are linear functions of the parameters. In practice this requirement is approximately satisfied in a region around the minimum of the χ^2 if the data are abundant and the minimum of the χ^2 lies far from any boundary of the parameters. Since in the case under consideration we are close to the boundary $\sin^2\vartheta_{13} \geq 0$, we can compare the Bayesian result with the frequentist least-squares result in which the boundary has not been taken into account only by relaxing the boundary restriction.

IV. AN INFORMATIVE PRIOR

In the previous section we analyzed the solar and KamLAND neutrino data assuming a constant uninformative prior probability distribution in the three-dimensional space of the parameters Δm^2_{21}, $\sin^2\vartheta_{12}$, and $\sin^2\vartheta_{13}$. However, as remarked in the introductory Sec. I, the value of ϑ_{13} was known to be small before the analysis of solar and KamLAND neutrino data from the negative results of the Chooz [6] and Palo Verde [7] long-baseline neutrino oscillation experiments combined with the evidence of neutrino oscillations in atmospheric and long-baseline accelerator neutrino experiments. In the Bayesian approach it is natural to try to express this prior knowledge through a prior probability distribution. The resulting posterior probability distribution of the mixing parameters Δm^2_{21}, $\sin^2\vartheta_{12}$, and $\sin^2\vartheta_{13}$ is interpreted as our knowledge about their values obtained from solar and KamLAND neutrino data, taking into account the information on ϑ_{13} obtained in atmospheric and long-baseline accelerator and reactor neutrino experiments.

Since we do not have the machinery for the fit of the data of atmospheric and long-baseline accelerator and reactor neutrino experiments, we constructed a prior probability distribution for ϑ_{13} using the χ^2 reported in Fig. 24 of Ref. [31], where such fit was performed. In Fig. 24 of Ref. [31] there are two slightly different curves corresponding to the normal and inverted schemes (see Fig. 1), which depict $\chi^2(\cos\delta \sin\vartheta_{13})$ for the two CP-conserving cases $\cos\delta = \pm 1$, where δ is the phase in the mixing matrix in Eq. (A2). Since we do not have any information on the value of δ, for each scheme we considered a prior probability distribution for ϑ_{13} marginalized over $\cos\delta = \pm 1$:

$$p(\vartheta_{13}|\mathcal{I}) \propto \sum_{\cos\delta=\pm 1} \exp\left(-\frac{\chi^2(\cos\delta \sin\vartheta_{13})}{2}\right). \qquad (4.1)$$

For $\sin^2\vartheta_{12}$ and Δm^2_{21} we assumed constant uninformative priors as in Sec. III.

The prior distributions (4.1) in the normal and inverted schemes are depicted by the dotted curves in Fig. 12, from which one can see that they have a maximum for $\sin^2\vartheta_{13} = 0$. Hence, they disfavor the hint of $\vartheta_{13} > 0$. The 90%, 95%, and 99.73% prior upper bounds for $\sin^2\vartheta_{13}$ are

$$\sin^2\vartheta_{13} < \begin{cases} 0.030, 0.036, 0.051 & \text{(normal scheme)}, \\ 0.033, 0.039, 0.057 & \text{(inverted scheme)}. \end{cases} \tag{4.2}$$

Notice that such disfavoring of the hint of $\vartheta_{13} > 0$ obtained from the χ^2 in Fig. 24 of Ref. [31] in the Bayesian approach is in contrast with a faint hint of $\vartheta_{13} > 0$ which can be obtained in the frequentist approach by considering the minimum of χ^2 at $\cos\delta \sin\vartheta_{13} \simeq -0.1$ and $\Delta\chi^2 \simeq 0.2$ at $\vartheta_{13} = 0$ (see the discussion in Ref. [31]). The contrast is due to the different marginalization procedures in the frequentist and Bayesian theories: in the frequentist theory only the minimum of χ^2 with respect to the marginalized parameters is considered, whereas in the Bayesian theory marginalization is implemented by integrating over the distribution of the marginalized parameters, as we have done, for example, in Eq. (3.3). In the case of the marginalization over $\cos\delta = \pm 1$, the Bayesian procedure of summing the prior probability distribution over $\cos\delta = \pm 1$ in Eq. (4.1) for each value of $\sin\vartheta_{13}$ is different from the frequentist consideration of $\chi^2(\sin\vartheta_{13})$ for $\cos\delta = -1$ only, which is due to $\chi^2(\sin\vartheta_{13}|\cos\delta = -1) < \chi^2(\sin\vartheta_{13}|\cos\delta = 1)$. In general, the Bayesian marginalization procedure has the merit to take into account all the distribution of the marginalized parameters, which gives more information than the single point of minimum of χ^2.

Using the informative prior on ϑ_{13} in Eq. (4.1), from the analysis of solar and KamLAND data We found the best-fit point, corresponding to the maximum of the posterior probability distribution,

$$\begin{gathered} \Delta m^2_{21} = 7.58 \times 10^{-5}\ \text{eV}^2, \qquad \sin^2\vartheta_{12} = 0.31, \\ \sin^2\vartheta_{13} = 0.012. \end{gathered} \tag{4.3}$$

The shadowed areas in Figs. 10 and 11 show the posterior credible regions with 90%, 95%, and 99.73% probability in the $\sin^2\vartheta_{13}$-Δm^2_{21} and $\sin^2\vartheta_{12}$-$\sin^2\vartheta_{13}$ planes, respectively. The boundaries of the corresponding regions obtained with an uninformative prior, shown in Figs. 5 and 6, are depicted with solid lines.

Since the prior information constrains only ϑ_{13}, the best-fit values and allowed ranges of Δm^2 and ϑ_{12} are similar to those obtained in Sec. III with an uninformative prior. A small change is due to the correlation with ϑ_{13}.

On the other hand, one can see that the assumption of the informative prior in Eq. (4.1) leads to a significant reduction of the allowed range of ϑ_{13} with respect to that obtained with an uninformative prior, as should have been expected.

A curious feature of Figs. 10 and 11 is that the 90% and 95% allowed ranges of $\sin^2\vartheta_{13}$ seem to be larger than those allowed by the prior distribution (vertical straight lines in Fig. 10 and horizontal straight lines in Fig. 11). Such a conclusion would be erroneous, because the prior distribution in Eq. (4.1) concerns only one parameter, whereas the credible regions in Figs. 10 and 11 constrain two parameters taking into account their correlation.

The posterior probability distribution of $\sin^2\vartheta_{13}$ obtained from the marginalization in Eq. (3.3) implies an allowed range of $\sin^2\vartheta_{13}$ which is smaller than that given by the prior distribution, as one can see from Fig. 12. We obtained the 90%, 95%, and 99.73% upper bounds

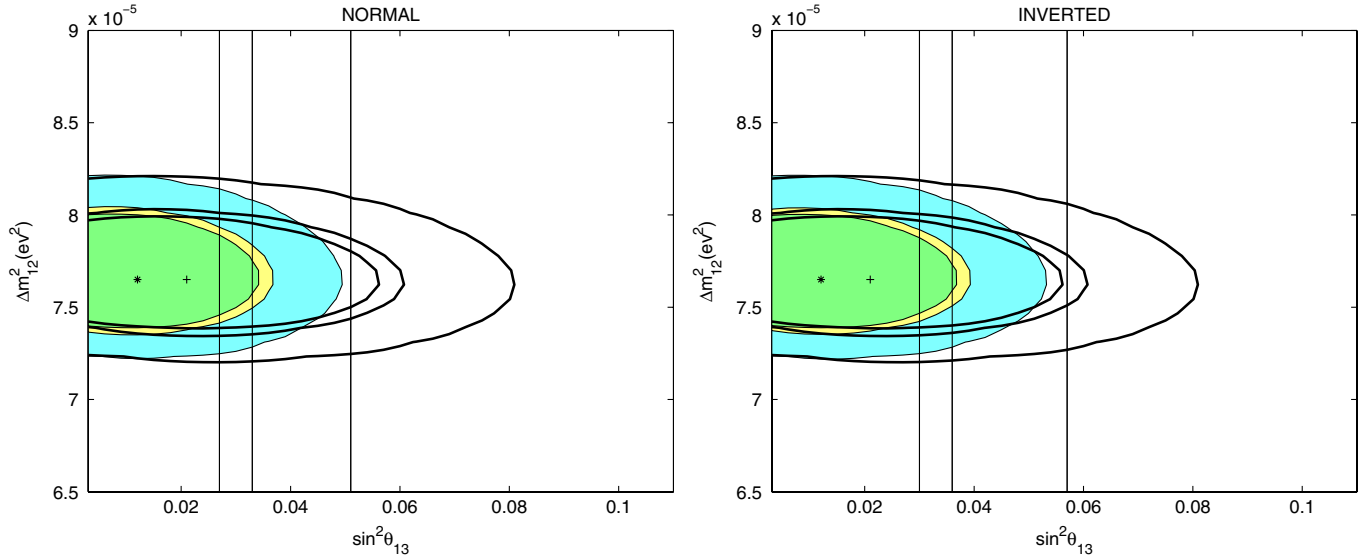

FIG. 10 (color online). Shadowed areas: 90%, 95%, and 99.73% Bayesian credible regions in the $\sin^2\vartheta_{13}$-Δm^2_{21} plane obtained with the informative prior probability distribution in Eq. (4.1). The regions enclosed by solid lines correspond to those in Fig. 5, obtained with an uninformative prior. The straight vertical dotted lines enclose, respectively, the 90%, 95%, and 99.73% prior credible regions of $\sin^2\vartheta_{13}$. The left and right plots correspond, respectively, to a normal and an inverted scheme (see Fig. 1). The cross and asterisk indicate, respectively, the best-fit points of the analyses with uninformative and informative priors.

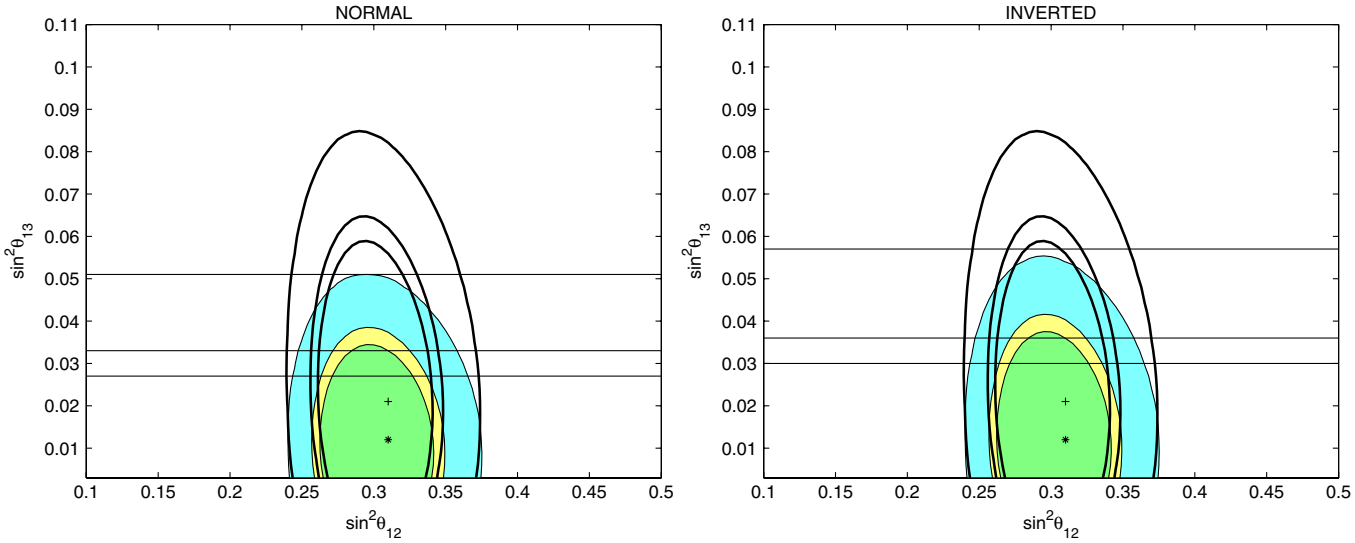

FIG. 11 (color online). Shadowed areas: 90%, 95%, and 99.73% Bayesian credible regions in the $\sin^2\vartheta_{12}$-$\sin^2\vartheta_{13}$ plane obtained with the informative prior probability distribution in Eq. (4.1). The regions enclosed by solid lines correspond to those in Fig. 6, obtained with an uninformative prior. The straight horizontal dotted lines enclose, respectively, the 90%, 95%, and 99.73% prior credible regions of $\sin^2\vartheta_{13}$. The left and right plots correspond, respectively, to a normal and an inverted scheme (see Fig. 1). The cross and asterisk indicate, respectively, the best-fit points of the analyses with uninformative and informative priors.

$$\sin^2\vartheta_{13} < \begin{cases} 0.027, 0.030, 0.045 & \text{(normal scheme)}, \\ 0.030, 0.033, 0.048 & \text{(inverted scheme)}, \end{cases} \tag{4.4}$$

which are smaller than the corresponding ones in Eq. (4.2). These bounds are also about 60% smaller than those obtained in Eq. (3.4) with an uninformative prior. Figure 13 shows the comparison of the posterior probability with the one in Fig. 9, which has been obtained with an uninformative flat prior.

It is interesting to note that the bounds on $\sin^2\vartheta_{13}$ in Eq. (4.4) are similar to those obtained with a global χ^2 analysis of neutrino oscillation data in Ref. [9] (see, however, the caveat on the comparison of frequentist and Bayesian results discussed at the end of Sec. III). Our results also agree with the weakening of the hint of $\vartheta_{13} > 0$ discussed in Ref. [9] coming from the addition of atmos-

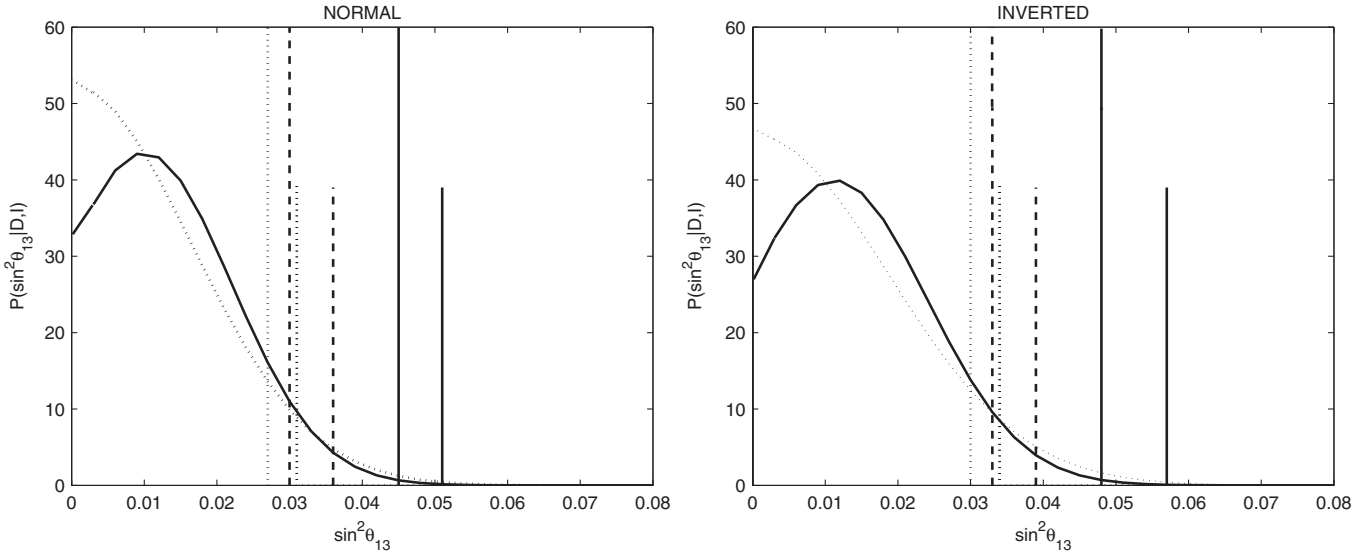

FIG. 12. Marginal posterior probability distribution of $\sin^2\vartheta_{13}$ obtained with the informative prior probability distribution in Eq. (4.1). The dotted curve shows the prior distribution in Eq. (4.1). The long (short) straight vertical lines show the 90%, 95%, and 99.73% posterior (prior) probability levels. The short straight dotted vertical lines have been slightly shifted to the right to avoid superposition [compare with Eqs. (4.2) and (4.4)].

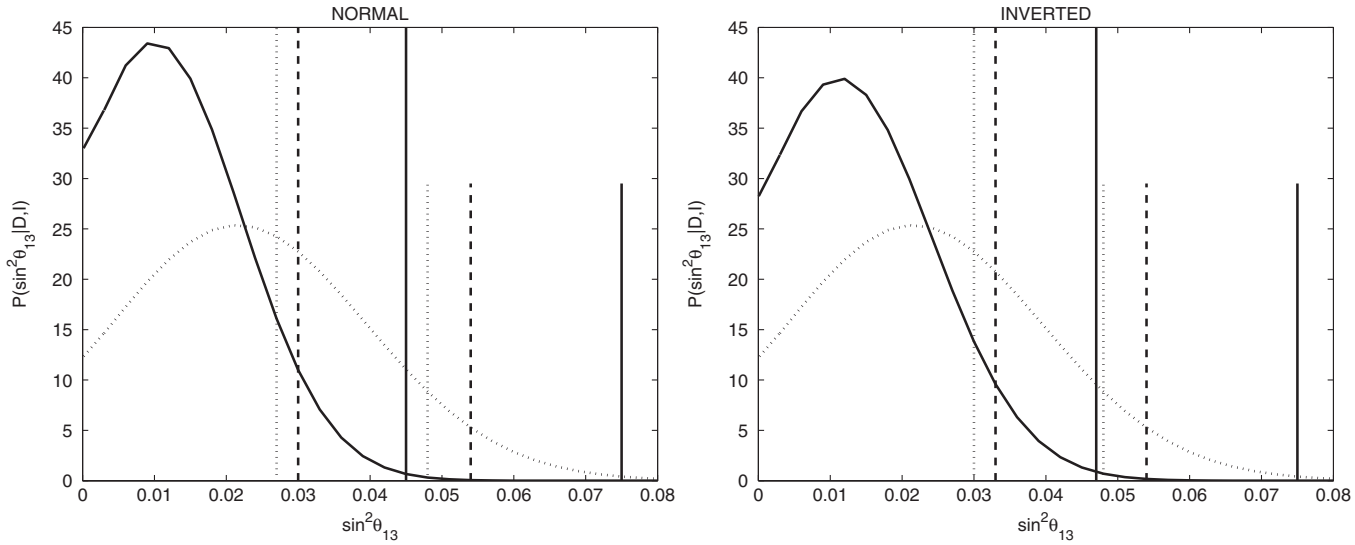

FIG. 13. Marginal posterior probability distribution of $\sin^2\vartheta_{13}$ obtained with the informative prior probability distribution in Eq. (4.1). The dotted curve shows the marginal posterior distribution in Fig. 9, obtained with an uninformative flat prior. The long straight vertical lines show the 90%, 95%, and 99.73% posterior probability levels in Eq. (4.4). The short straight vertical lines show the corresponding probability levels in Eq. (3.4), obtained with an uninformative flat prior. The short straight dotted vertical line in the figure on the right has been slightly shifted to the right to avoid superposition [compare with Eqs. (3.4) and (4.4)].

pheric and long-baseline accelerator and reactor neutrino data to the analysis of solar and KamLAND data: using the method described in Sec. III, the significance of the hint of $\vartheta_{13} > 0$ is reduced from about 1.2σ to about 0.8σ (with 0.72 and 0.75 respective probabilities of the smallest posterior credible region which includes $\vartheta_{13} = 0$ in the normal and inverted schemes). The discrepancy with the 1.6σ reported in Ref. [27] is probably due to the marginalization over $\cos\delta = \pm 1$ in Eq. (4.1). In fact, for $\cos\delta = -1$ Fig. 24 of Ref. [31] implies a prior in favor of $\vartheta_{13} > 0$, which leads to a global hint of $\vartheta_{13} > 0$ at the 1.5σ level (with 0.93 probability of the smallest posterior credible region which includes $\vartheta_{13} = 0$), in agreement with the value in Ref. [27] (1.6σ). Let us however emphasize that, since the marginalization over the unknown value of δ is the correct procedure in the Bayesian approach, our result for the statistical significance of the global hint of $\vartheta_{13} > 0$ is 0.8σ.

Let us finally remark that the results presented in this section depend on the choice of the prior probability distribution for ϑ_{13} obtained from the fit of the data of atmospheric and long-baseline accelerator and reactor neutrino experiments. In Eq. (4.1), instead of the χ^2 of Ref. [31] we could have used, for example, the χ^2 of one of Refs. [9,32–34]. However, since in these papers the same data have been fitted with similar assumptions and methods, using one of these χ^2's would not change dramatically the numerical results presented above. For example, we considered the χ^2 in Fig. 3 of Ref. [9], which corresponds to the prior upper bounds

$$\sin^2\vartheta_{13} < 0.030(90\%), \quad 0.039(95\%), \quad 0.063(99.73\%). \tag{4.5}$$

We obtained the best-fit values

$$\Delta m^2_{21} = 7.58 \times 10^{-5}\ \text{eV}^2, \quad \sin^2\vartheta_{12} = 0.31, \quad \sin^2\vartheta_{13} = 0.008, \tag{4.6}$$

and the posterior upper limits

$$\sin^2\vartheta_{13} < 0.030(90\%), \quad 0.033(95\%), \quad 0.051(99.73\%). \tag{4.7}$$

One can see that these values are close to the corresponding ones in Eqs. (4.2), (4.3), and (4.4). For the hint of $\vartheta_{13} > 0$ we have a 0.9σ statistical significance (with 0.78 probability of the smallest posterior credible region which includes $\vartheta_{13} = 0$), in perfect agreement with Ref. [9].

V. CONCLUSIONS

In this paper we presented the results of a Bayesian analysis of the solar and KamLAND neutrino data with the aim of determining the value of the unknown mixing angle ϑ_{13} in the framework of three-neutrino mixing.

We found that with an uninformative flat prior distribution in the relevant mixing parameters Δm^2_{12}, $\sin^2\vartheta_{12}$, $\sin^2\vartheta_{13}$, the Bayesian credible regions in the $\sin^2\vartheta_{13}$-Δm^2_{12} and $\sin^2\vartheta_{12}$-$\sin^2\vartheta_{13}$ planes are only slightly smaller than the allowed regions obtained with a traditional least-squares analysis, implying a rather stringent upper

bound for $\sin^2\vartheta_{13}$. Our analysis confirms the 1.2σ hint of $\vartheta_{13} > 0$ found in Ref. [27].

We also performed an analysis with an informative prior which represents information on ϑ_{13} obtained in atmospheric and long-baseline accelerator and reactor neutrino experiments, independently from solar and KamLAND neutrino data. We found that such a prior implies a significant decrease of the upper bound on ϑ_{13} with respect to that obtained with an uninformative prior and the hint of $\vartheta_{13} > 0$ is reduced to a 0.8σ level. Our results are similar to those obtained with a global χ^2 analysis of neutrino oscillation data in Ref. [9] (see, however, the caveat on the comparison of frequentist and Bayesian results discussed at the end of Sec. III).

Let us finally emphasize that Bayesian inference (see Refs. [35–39]) is founded on a consistent theory and can always be implemented in a correct way (given enough computational power). On the other hand, the frequentist method is based on an unphysical definition of probability and in most cases of interest cannot be implemented in a correct way. In particular, a dramatic flaw of the frequentist method is that the frequentist definition of probability does not allow the treatment of theoretical and systematic errors as random variables. Hence, the aim of the frequentist statistics approach of extracting objective statistical information from data cannot be realized in practice. Since the Bayesian theory does not suffer from such shortcomings, we think that it is preferable for attaining reliable results from the analysis of experimental data.

ACKNOWLEDGMENTS

C. Giunti would like to thank the Department of Theoretical Physics of the University of Torino for hospitality and support.

APPENDIX: REGENERATION OF SOLAR ν_e'S IN THE EARTH

Solar neutrinos arriving at a detector during nighttime pass through the Earth, where the matter effect (also called "MSW effect" [40,41]) can cause a change in the flavor composition, which is called "regeneration of solar ν_e's in the Earth." In this appendix, we derive the connection between the averaged probability of survival of solar electron neutrinos passing through the Earth, $\bar{P}^{\text{Sun+Earth}}_{\nu_e\to\nu_e}$, which is measured during nighttime, the averaged probability of ν_e survival from the core of the Sun to the surface of the Earth, $\bar{P}^{\text{Sun}}_{\nu_e\to\nu_e}$, which is measured during daytime, and the probability of $\nu_2 \to \nu_e$ transitions in the Earth, $P^{\text{Earth}}_{\nu_2\to\nu_e}$. We also discuss the connection between $P^{\text{Earth}}_{\nu_2\to\nu_e}$ in the case of three-neutrino mixing and the probability of $\nu_2 \to \nu_e$ transitions in the Earth in the case of two-neutrino mixing.

The mixing of neutrino states is given by

$$|\nu_\alpha\rangle = \sum_{k=1}^{3} U^*_{\alpha k}|\nu_k\rangle \qquad (\alpha = e, \mu, \tau), \tag{A1}$$

where U is the 3×3 unitary mixing matrix of the neutrino fields (see Refs. [1–3]). We adopt the standard parametrization [4,5]

$$U = \begin{pmatrix} c_{12}c_{13} & s_{12}c_{13} & s_{13}e^{-i\delta} \\ -s_{12}c_{23} - c_{12}s_{23}s_{13}e^{i\delta} & c_{12}c_{23} - s_{12}s_{23}s_{13}e^{i\delta} & s_{23}c_{13} \\ s_{12}s_{23} - c_{12}c_{23}s_{13}e^{i\delta} & -c_{12}s_{23} - s_{12}c_{23}s_{13}e^{i\delta} & c_{23}c_{13} \end{pmatrix}, \tag{A2}$$

where $c_{ab} \equiv \cos\vartheta_{ab}$ and $s_{ab} \equiv \sin\vartheta_{ab}$. The three mixing angles ϑ_{12}, ϑ_{13}, ϑ_{23} take values in the ranges $0 \le \vartheta_{ab} \le \pi/2$. The CP-violating phase δ is confined in the interval $0 \le \delta < 2\pi$. We neglected possible Majorana phases, which are irrelevant for neutrino oscillations [42–44].

A solar neutrino, created in the core of the Sun as a ν_e, arrives in a detector as a superposition of ν_1, ν_2, and ν_3. However, since the neutrino squared-mass differences are relatively large [ee Eqs. (1.1), (1.2), (1.3), (1.4), and (1.5)], the average of the oscillation probability over the energy resolution of the detector washes out the interference terms between the massive neutrinos [45]. This is due to the fact that the vacuum oscillation lengths are much shorter than the Sun–Earth distance:

$$\begin{aligned} L^{\text{osc}}_{21} &= \frac{4\pi E}{\Delta m^2_{21}} \simeq 30\ \text{km}\left(\frac{E}{\text{MeV}}\right), \\ L^{\text{osc}}_{32} &\simeq L^{\text{osc}}_{31} = \frac{4\pi E}{|\Delta m^2_{31}|} \simeq 1\ \text{km}\left(\frac{E}{\text{MeV}}\right), \end{aligned} \tag{A3}$$

where E is the neutrino energy, which in solar neutrino experiments varies in the interval

$$0.2\ \text{MeV} \lesssim E \lesssim 15\ \text{MeV}. \tag{A4}$$

Then, the measurable averaged survival probability of solar electron neutrinos after crossing the Earth is given by

$$\bar{P}^{\text{Sun+Earth}}_{\nu_e\to\nu_e} = \sum_{k=1}^{3} P^{\text{Sun}}_{\nu_e\to\nu_k} P^{\text{Earth}}_{\nu_k\to\nu_e}, \tag{A5}$$

where $P^{\text{Sun}}_{\nu_e\to\nu_k}$ is the probability of $\nu_e \to \nu_k$ transitions from the solar core to the surface of the Earth and $P^{\text{Earth}}_{\nu_k\to\nu_e}$ is the probability of $\nu_k \to \nu_e$ transitions in the passage through the Earth.

In matter, electron neutrinos feel a charged-current potential $V_{\text{CC}} = \sqrt{2}G_F N_e$, where G_F is the Fermi constant and N_e is the electron number density. The quantity which gives the matter effect in the evolution equation of neutrino flavors is

$$A_{\rm CC} = 2EV_{\rm CC} = 1.53 \times 10^{-7}\ {\rm eV}^2 \left(\frac{N_e}{N_A\ {\rm cm}^{-3}}\right)\left(\frac{E}{\rm MeV}\right), \tag{A6}$$

where N_A is the Avogadro number. The electron number density in the solar core is about $100N_A$ cm^{-3}. In the Earth, the electron number density varies from about $2.2N_A$ cm^{-3} in the mantle to about $5.5N_A$ cm^{-3} in the core. Thus, for solar neutrinos we have $A_{\rm CC} \lesssim 2.3 \times 10^{-4}$ eV^2, which is much smaller than the atmospheric squared-mass difference $\Delta m^2_{\rm ATM}$ [see Eq. (1.2)]. This means that the matter effect cannot induce transitions between ν_3 and the two neutrinos ν_1 and ν_2, since the two groups are separated by the large atmospheric squared-mass difference $\Delta m^2_{\rm ATM}$ [see Eq. (1.5) and Fig. 1]. In other words, the massive neutrino component ν_3 propagates without disturbance from the core of the Sun to the detector and the corresponding transition probabilities in Eq. (A5) are simply given by

$$P^{\rm Sun}_{\nu_e\to\nu_3} = P^{\rm Earth}_{\nu_3\to\nu_e} = |\langle\nu_3|\nu_e\rangle|^2 = |U_{e3}|^2. \tag{A7}$$

Furthermore, taking into account the conservation of probability, we have

$$P^{\rm Sun}_{\nu_e\to\nu_1} = 1 - P^{\rm Sun}_{\nu_e\to\nu_3} - P^{\rm Sun}_{\nu_e\to\nu_2} = 1 - |U_{e3}|^2 - P^{\rm Sun}_{\nu_e\to\nu_2}, \tag{A8}$$

$$P^{\rm Earth}_{\nu_1\to\nu_e} = 1 - P^{\rm Earth}_{\nu_3\to\nu_e} - P^{\rm Earth}_{\nu_2\to\nu_e} = 1 - |U_{e3}|^2 - P^{\rm Earth}_{\nu_2\to\nu_e}. \tag{A9}$$

Let us now express the averaged survival probability $\bar{P}^{\rm Sun}_{\nu_e\to\nu_e}$ of electron neutrinos from the solar core to the surface of the Earth in terms of the transition probabilities $P^{\rm Sun}_{\nu_e\to\nu_k}$:

$$\bar{P}^{\rm Sun}_{\nu_e\to\nu_e} = \overline{|\langle\nu_e|\mathcal{S}|\nu_e\rangle|^2} = \overline{\left|\sum_{k=1}^{3}\langle\nu_e|\nu_k\rangle\langle\nu_k|\mathcal{S}|\nu_e\rangle\right|^2} = \sum_{k=1}^{3}|U_{ek}|^2 P^{\rm Sun}_{\nu_e\to\nu_k}, \tag{A10}$$

where $\mathcal{S}$ is the evolution operator. We neglected the interference terms for the reason discussed above, before Eq. (A5). Using Eqs. (A7), (A8), and (A10), we can express $P^{\rm Sun}_{\nu_e\to\nu_2}$ in terms of $\bar{P}^{\rm Sun}_{\nu_e\to\nu_e}$:

$$P^{\rm Sun}_{\nu_e\to\nu_2} = \frac{|U_{e1}|^2(1-|U_{e3}|^2) + |U_{e3}|^4 - \bar{P}^{\rm Sun}_{\nu_e\to\nu_e}}{|U_{e1}|^2 - |U_{e2}|^2}. \tag{A11}$$

Finally, using Eqs. (A7)–(A9) and (A11), we obtain, from Eq. (A5),

$$\bar{P}^{\rm Sun+Earth}_{\nu_e\to\nu_e} = \bar{P}^{\rm Sun}_{\nu_e\to\nu_e} + \frac{[(1-|U_{e3}|^2)^2 - 2(\bar{P}^{\rm Sun}_{\nu_e\to\nu_e} - |U_{e3}|^4)][P^{\rm Earth}_{\nu_2\to\nu_e} - |U_{e2}|^2]}{|U_{e1}|^2 - |U_{e2}|^2}. \tag{A12}$$

Since in practice $|U_{e1}|^2 > |U_{e2}|^2$, because $\sin^2\vartheta_{12} < 1$ (see Refs. [10,31]), and $|U_{e3}|^2$ is small, there is a regeneration of electron neutrinos in the Earth if $P^{\rm Earth}_{\nu_2\to\nu_e} > |U_{e2}|^2$. Note that in the absence of matter effects, we have $P^{\rm Earth}_{\nu_2\to\nu_e} = |\langle\nu_2|\nu_e\rangle|^2 = |U_{e2}|^2$ and $\bar{P}^{\rm Sun+Earth}_{\nu_e\to\nu_e} = \bar{P}^{\rm Sun}_{\nu_e\to\nu_e}$.

Let us now discuss the calculation of $P^{\rm Earth}_{\nu_2\to\nu_e}$. The evolution of neutrino flavors in matter is governed by the Schrödinger equation (see Refs. [1–3])

$$i\frac{d}{dx}\Psi_F = \mathbb{H}_F\Psi_F, \tag{A13}$$

with the effective Hamiltonian

$$\mathbb{H}_F = \frac{1}{2E}(U\Delta\mathbb{M}^2U^\dagger + \mathbb{A}), \tag{A14}$$

and

$$\Psi_F \equiv \begin{pmatrix}\psi_e\\ \psi_\mu\\ \psi_\tau\end{pmatrix}, \qquad \Delta\mathbb{M}^2 \equiv \begin{pmatrix}0 & 0 & 0\\ 0 & \Delta m^2_{21} & 0\\ 0 & 0 & \Delta m^2_{31}\end{pmatrix}, \qquad \mathbb{A} \equiv \begin{pmatrix}A_{\rm CC} & 0 & 0\\ 0 & 0 & 0\\ 0 & 0 & 0\end{pmatrix}. \tag{A15}$$

Here, $\psi_\alpha = \langle\nu_\alpha|\nu\rangle$ is the amplitude of the flavor α in the state $|\nu\rangle$ which describes a propagating neutrino. The column matrix Ψ_F of flavor amplitudes is related to the column matrix $\Psi_M \equiv (\psi_1, \psi_2, \psi_3)^T$ of mass amplitudes $(\psi_k = \langle\nu_k|\nu\rangle)$ by

$$\Psi_F = U\Psi_M. \tag{A16}$$

In the calculation of $P^{\rm Earth}_{\nu_2\to\nu_e}$, the initial mass and flavor amplitudes are

$$\psi_k(0) = \delta_{k2}, \qquad \psi_\alpha(0) = U_{\alpha 2}. \tag{A17}$$

The probability of $\nu_2 \to \nu_e$ transitions at a distance x from neutrino production is given by

$$P_{\nu_2\to\nu_e}(x) = |\psi_e(x)|^2. \tag{A18}$$

Taking into account the fact that the mixing matrix in the parametrization in Eq. (A2) can be written as

$$U = R^{23} W^{13} R^{12}, \tag{A19}$$

with

$$R^{12} = \begin{pmatrix} c_{12} & s_{12} & 0 \\ -s_{12} & c_{12} & 0 \\ 0 & 0 & 1 \end{pmatrix}, \qquad R^{23} = \begin{pmatrix} 1 & 0 & 0 \\ 0 & c_{23} & s_{23} \\ 0 & -s_{23} & c_{23} \end{pmatrix},$$
$$W^{13} = \begin{pmatrix} c_{13} & 0 & s_{13}e^{-i\delta} \\ 0 & 1 & 0 \\ -s_{13}e^{i\delta} & 0 & c_{13} \end{pmatrix}, \tag{A20}$$

it is convenient to work with the new column matrix of amplitudes $\hat{\Psi} \equiv (\hat{\psi}_1, \hat{\psi}_2, \hat{\psi}_3)^T$ defined by

$$\hat{\Psi} = W^{13\dagger} R^{23\dagger} \Psi_F = R^{12} \Psi_M, \tag{A21}$$

which follows the evolution equation

$$i\frac{d}{dx}\hat{\Psi} = \hat{\mathbb{H}}\,\hat{\Psi}. \tag{A22}$$

Since R^{23} commutes with the matter potential matrix $\mathbb{A}$, the new effective Hamiltonian $\hat{\mathbb{H}}$ is given by

$$\hat{\mathbb{H}} = \frac{1}{2E}(R^{12}\Delta\mathbb{M}^2 R^{12\dagger} + W^{13\dagger}\mathbb{A}W^{13}). \tag{A23}$$

Explicitly, we have

$$\hat{\mathbb{H}} = \frac{1}{2E}\begin{pmatrix} s_{12}^2\Delta m_{21}^2 + c_{13}^2 A_{\rm CC} & c_{12}s_{12}\Delta m_{21}^2 & -c_{13}s_{13}e^{-i\delta}A_{\rm CC} \\ c_{12}s_{12}\Delta m_{21}^2 & c_{12}^2\Delta m_{21}^2 & 0 \\ -c_{13}s_{13}e^{i\delta}A_{\rm CC} & 0 & \Delta m_{31}^2 + s_{13}^2 A_{\rm CC} \end{pmatrix}. \tag{A24}$$

From Eq. (A21), we have $\hat{\psi}_3 = \psi_3$. Therefore, $\hat{\psi}_3$ is the amplitude of ν_3. Since $\Delta m_{31}^2 \gg A_{\rm CC}$, in practice the third eigenvalue of $\hat{\mathbb{H}}$ is equal to $\Delta m_{31}^2/2E$ and the matter effect cannot induce transitions between ν_3 and the other two massive neutrinos, as discussed above. Furthermore, since $\hat{\psi}_3(0) = \psi_3(0) = 0$ [from Eq. (A17)], in practice the contribution of ν_3 is negligible and $P^{\rm Earth}_{\nu_2\to\nu_e}$ can be calculated by solving the effective two-neutrino evolution equation

$$i\frac{d}{dx}\tilde{\Psi} = \tilde{\mathbb{H}}\,\tilde{\Psi}, \tag{A25}$$

with $\tilde{\Psi} \equiv (\tilde{\psi}_1, \tilde{\psi}_2)^T = (\hat{\psi}_1, \hat{\psi}_2)^T$ and

$$\tilde{\mathbb{H}} = \frac{1}{2E}\begin{pmatrix} s_{12}^2\Delta m_{21}^2 + c_{13}^2 A_{\rm CC} & c_{12}s_{12}\Delta m_{21}^2 \\ c_{12}s_{12}\Delta m_{21}^2 & c_{12}^2\Delta m_{21}^2 \end{pmatrix}. \tag{A26}$$

This effective Hamiltonian coincides with the effective Hamiltonian in the case of two-neutrino mixing (see Refs. [1–3]), with the matter contribution $A_{\rm CC}$ multiplied by the three-neutrino mixing factor c_{13}^2. The initial column matrix of amplitudes is explicitly given, from Eqs. (A17) and (A21), by

$$\tilde{\Psi}(0) = \begin{pmatrix} c_{12} & s_{12} \\ -s_{12} & c_{12} \end{pmatrix}\begin{pmatrix} 0 \\ 1 \end{pmatrix} = \begin{pmatrix} s_{12} \\ c_{12} \end{pmatrix}. \tag{A27}$$

The probability of $\nu_2 \to \nu_e$ transitions at a distance x from neutrino production is given by

$$P_{\nu_2\to\nu_e}(x) = |[R^{23}W^{13}\hat{\Psi}(x)]_e|^2 = c_{13}^2|\tilde{\psi}_1(x)|^2. \tag{A28}$$

Therefore, in practice, the probability of $\nu_2 \to \nu_e$ transitions in the Earth is given by

$$P^{\rm Earth}_{\nu_2\to\nu_e} = (1 - |U_{e3}|^2)P^{{\rm Earth};2\nu}_{\nu_2\to\nu_e}, \tag{A29}$$

where $P^{{\rm Earth};2\nu}_{\nu_2\to\nu_e}$ is the probability of $\nu_2 \to \nu_e$ transitions calculated in the case of two-neutrino mixing with an effective matter contribution multiplied by $c_{13}^2 = 1 - |U_{e3}|^2$.

[1] S. M. Bilenky, C. Giunti, and W. Grimus, Prog. Part. Nucl. Phys. **43**, 1 (1999).
[2] C. Giunti and M. Laveder, in *Developments in Quantum Physics—2004*, edited by F. Columbus and V. Krasnoholovets (Nova Science, Hauppauge, New York, 2003), p. 197.
[3] C. Giunti and C. W. Kim, *Fundamentals of Neutrino Physics and Astrophysics* (Oxford University, New York, 2007).
[4] L. L. Chau and W. Y. Keung, Phys. Rev. Lett. **53**, 1802 (1984).
[5] W. M. Yao *et al.*, J. Phys. G **33**, 1 (2006).
[6] M. Apollonio *et al.* (Chooz Collaboration), Eur. Phys. J. C **27**, 331 (2003).
[7] F. Boehm *et al.* (Palo Verde Collaboration), Phys. Rev. D **64**, 112001 (2001).
[8] S. M. Bilenky and C. Giunti, Phys. Lett. B **444**, 379 (1998).

[9] T. Schwetz, M. Tortola, and J. W. F. Valle, New J. Phys. **10**, 113011 (2008).
[10] B. L. Chen *et al.*, Mod. Phys. Lett. A **21**, 2269 (2006).
[11] B. T. Cleveland *et al.*, Astrophys. J. **496**, 505 (1998).
[12] M. Altmann *et al.* (GNO Collaboration), Phys. Lett. B **616**, 174 (2005).
[13] J. N. Abdurashitov *et al.* (SAGE Collaboration), J. Exp. Theor. Phys. **95**, 181 (2002).
[14] J. Hosaka *et al.* (Super-Kamkiokande Collaboration), Phys. Rev. D **73**, 112001 (2006).
[15] J. Cravens *et al.* (Super-Kamiokande Collaboration), Phys. Rev. D **78**, 032002 (2008).
[16] B. Aharmim *et al.* (SNO Collaboration), Phys. Rev. C **72**, 055502 (2005).
[17] B. Aharmim *et al.* (SNO Collaboration), Phys. Rev. Lett. **101**, 111301 (2008).
[18] G. L. Fogli and E. Lisi, Astropart. Phys. **3**, 185 (1995).
[19] G. L. Fogli *et al.*, Phys. Rev. D **62**, 013002 (2000).
[20] M. V. Garzelli and C. Giunti, Phys. Lett. B **488**, 339 (2000).
[21] M. V. Garzelli and C. Giunti, J. High Energy Phys. 12 (2001) 017.
[22] J. N. Bahcall and M. H. Pinsonneault, Phys. Rev. Lett. **92**, 121301 (2004).
[23] X. Shi and D. N. Schramm, Phys. Lett. B **283**, 305 (1992).
[24] S. Abe *et al.* (KamLAND Collaboration), Phys. Rev. Lett. **100**, 221803 (2008).
[25] S. Baker and R. D. Cousins, Nucl. Instrum. Methods Phys. Res., Sect. A **221**, 437 (1984).
[26] M. Maltoni, T. Schwetz, and J. Valle, Phys. Rev. D **67**, 093003 (2003).
[27] G. Fogli *et al.*, Phys. Rev. Lett. **101**, 141801 (2008).
[28] A. B. Balantekin and D. Yilmaz, J. Phys. G **35**, 075007 (2008).
[29] F. James, *Statistical Methods in Experimental Physics* (World Scientific, Singapore, 2006).
[30] C. Amsler *et al.*, Phys. Lett. B **667**, 1 (2008).
[31] G. L. Fogli *et al.*, Prog. Part. Nucl. Phys. **57**, 742 (2006).
[32] M. C. Gonzalez-Garcia and M. Maltoni, Phys. Rep. **460**, 1 (2008).
[33] J. Escamilla, D. C. Latimer, and D. J. Ernst, arXiv: 0805.2924.
[34] A. Bandyopadhyay *et al.*, arXiv:0804.4857.
[35] H. Jeffreys, *Theory of Probability* (Oxford University, New York, 1961), first published in 1939.
[36] T. J. Loredo, in *Maximum-Entropy and Bayesian Methods, Dartmouth, 1989*, edited by P. Fougere (Kluwer Academic, Dordrecht, The Netherlands, 1990), p. 81.
[37] T. J. Loredo, in *Statistical Challenges in Modern Astronomy*, edited by E. D. Feigelson and G. J. Babu (Springer-Verlag, New York, 1992), p. 275.
[38] E. T. Jaynes, *Probability Theory: The Logic of Science* (Cambridge University Press, Cambridge, England, 2003).
[39] G. D'Agostini, *Bayesian Reasoning in Data Analysis, A Critical Introduction* (World Scientific, Singapore, 2003).
[40] L. Wolfenstein, Phys. Rev. D **17**, 2369 (1978).
[41] S. P. Mikheev and A. Y. Smirnov, Nuovo Cimento Soc. Ital. Fis. C **9**, 17 (1986).
[42] S. M. Bilenky, J. Hosek, and S. T. Petcov, Phys. Lett. **94B**, 495 (1980).
[43] M. Doi *et al.*, Phys. Lett. **102B**, 323 (1981).
[44] P. Langacker *et al.*, Nucl. Phys. **B282**, 589 (1987).
[45] A. S. Dighe, Q. Y. Liu, and A. Y. Smirnov, arXiv:hep-ph/ 9903329.